Scientific Reports

https://doi.org/10.1038/s41598-026-39341-6

Article in Press

Instability mechanism of deeply buried coal seam floor under mining effects and optimization of extraction roadway layout

Received: 20 December 2025

Accepted: 4 February 2026

Published online: 12 February 2026

Cite this article as: Chen X., Ma R., Zhou Y. *et al.* Instability mechanism of deeply buried coal seam floor under mining effects and optimization of extraction roadway layout. *Sci Rep* (2026). https://doi.org/10.1038/s41598-026-39341-6

Xueya Chen, Riming Ma, Yuejin Zhou, Jianfeng Li, Yunong Xu & Jichu Chen

Instability Mechanism of Deeply Buried Coal Seam Floor under Mining Effects and Optimization of Extraction Roadway Layout

Xueya Chen [1], Riming Ma [3], * Yuejin Zhou [3], * , Jianfeng Li [2] , Yunong Xu [3]and Jichu Chen [3]

[1]Shanxi Linxian Huarun Liansheng Huangjiagou Coal Industry Co.,Ltd., Jinzhong 045300,China
[2] Xuzhou Mining Group Co., Ltd., Xuzhou 221000, China
[3] State Key Laboratory for Geomechanics & Deep Underground Engineering Xuzhou, China University of Mining & Technology, Xuzhou 221116, China

*****Correspondence: ts25030014a31@cumt.edu.cn (R.M.); yuejinzh@163.com (Y.Z.);

Abstract: Mining-induced stress redistribution leads to rock deformation, fracture propagation, gas outflow, and floor water inrush, which present significant challenges for the layout of extraction roadways. To optimize the layout in deeply buried coal seams, a stress distribution model for the floor under mining effects was developed based on semi-infinite body theory. This model elucidates the characteristics of floor stress distribution. Simulations were conducted to analyze surrounding rock stress in extraction roadways with various layouts, resulting in a proposed optimized configuration through comparative analysis. The principal findings are as follows: (1) The floor stress model indicates that vertical stress decreases with depth, exhibiting a notable reduction after reaching 5 meters below the floor. (2) Numerical results align closely with theoretical patterns; specifically, vertical stress forms an "M" shape within the goaf while peak stresses diminish as depth increases. Maximum decay of vertical stress occurs at approximately 10 meters beneath the floor. (3) Vertical stress peaks reach their minimum value of 10.55 MPa when the inner offset coal pillar measures 30 meters; similarly, horizontal stress peaks are minimized at 19.37 MPa with an outer offset also set at 30 meters. Notably, the failure zone is smallest—approximately 2 meters—when employing this outer offset arrangement. (4) The optimized layout positions the extraction roadway at a depth of 17 meters below the floor while maintaining a coal pillar with an outer offset of 30 meters. (5) Monitoring efforts conducted at a Shanxi coal mine revealed that the failure range extended to only 1.9 meters, corroborating theoretical predictions and indicating no significant deformations occurred. This study provides a robust theoretical foundation for determining optimal positioning of extraction roadways within

deeply buried coal seams and serves as a valuable reference for analogous mining projects.

Keywords: Mining Influence; Strata behaviors; Extraction roadway; Deeply buried coal seam; Location selection

1 Introduction

Mining-induced stress during coal extraction significantly alters the floor stress field, leading to fracture propagation, instability of surrounding rock, and water inrush events, which can easily result in roadway instability [1-5]. Extraction roadways are typically situated below the working face to mitigate the risk of gas disasters. However, mining-induced stress modifies the stress field, causing previously balanced rock masses to experience uneven stresses. This condition can trigger fractures in the surrounding rock, slippage, and deformation, potentially culminating in surrounding rock instability. Such issues are particularly pronounced under conditions of great depth and high stress, where the plastic zone of the surrounding rock expands rapidly. This expansion results in a loss of support for adjacent rock layers, thereby increasing both complexity and difficulty within the support system. Optimizing the layout of extraction roadways in high-stress environments is essential for enhancing mining safety and ensuring roadway stability [6-10]. Consequently, it is imperative to investigate the characteristics of stress distribution and optimize extraction roadway layouts under mining-induced stress conditions prevalent in deep coal seams.

In-depth research and analysis of the failure characteristics of the surrounding rock from the perspective of the variation in the stress field of the working face floor under mining-induced effects can disclose the deformation mechanisms and identify the failure modes. This holds significant theoretical significance for exploring the rationality of the layout of floor drainage roadways. A considerable amount of research has been carried out both domestically and internationally on floor stress distribution and failure depth. Minggao Qian [11] proposed a block "voussoir beam" structural model based on floor failure conditions and utilized limit theory to analyze the failure load and maximum deformation points of the floor under different boundary conditions. He also applied "S-R" stability theory to assess the stability and failure range of the block structure after failure. Chunwang Zhang [12] conducted numerical analyses to explore the relationship between roadway deformation and interlayer slippage structures and examined how stress distribution and the evolution of key geological fractures influenced roadway stability under mining-induced stress. Hualei Zhang [13] employed semi-infinite body theory to establish a mechanical model for the stress

state of the mining-affected zone and derived a formula for calculating the width of the plastic zone in the surrounding rock under non-hydrostatic pressure. Lianguo Wang [14] developed a spatial semi-infinite body model and derived a formula for calculating the vertical stress in the floor. He combined theoretical analysis with microseismic monitoring to investigate stress distribution and the depth of floor failure after coal mining. Shenghu Luo [15] utilized physical similarity material experiments to study the deformation and failure evolution in steeply inclined coal seam groups and used numerical simulations to analyze the evolution of mining-induced stress transfer in the surrounding rock. Jun Wang [16] employed UDEC simulations to investigate the deformation and failure patterns of the surrounding rock in shallow multi-seam mining. Suimu Yang [17] used FLAC3D software to simulate the stress conditions under various drainage roadway layouts and, based on the simulation results, discussed the optimal strata arrangement for the floor drainage roadway. Can Zhao [18] utilized laboratory experiments, numerical simulations, and field testing to study the floor stress distribution, pressure relief range, and gas drainage layout in closely spaced coal seam mining and proposed a suitable drainage roadway layout. Zhu Tang [19] utilized FLAC3D simulations to optimize two drainage roadway layout schemes based on vertical stress and plastic failure zone analysis. Zhiwei Liu [20] applied slip line field theory and FLAC3D simulations to determine the drainage roadway layout in high-gas coal seams at Xintian coal mine.Yong'en Li [21] conducted theoretical analysis and numerical simulations to investigate the failure patterns of the surrounding rock and the optimal positioning of floor drainage roadways in deep confined water areas. At the level of mechanical theory, the poroelastic analytical solutions for a semi-permeable borehole within transversely isotropic media under non-hydrostatic in-situ stresses were rigorously investigated, providing essential theoretical criteria for the assessment of borehole stability in deep and complex formations[24-27]. In the realm of engineering technology, aiming to mitigate the hazards of intense ground pressure triggered by hard roofs in extra-thick coal seams, the weakening effects of horizontal hydraulic fracturing and multi-strata ground fracturing on rock breakage characteristics were systematically studied, thereby elucidating the physical mechanisms underlying precise stress regulation via the modification of overlying strata structures[28-29].

The aforementioned studies mainly concentrate on the stress distribution characteristics of the floor in deep or mining-impacted coal seams and the layout of the extraction roadway. Nevertheless, there is a dearth of systematic research on the optimization of the extraction roadway location under high ground stress and the combined effects of mining-induced stress. Hence, this paper takes the gas drainage requirements of an extraction roadway in a coal mine

in Shanxi as the starting point. Firstly, through the theoretical calculation of the floor stress in the working face, the relationship between the floor stress and the depth beneath the floor is derived. Subsequently, FLAC3D numerical simulations are employed to study the stress distribution in the floor of the working face and the surrounding rock stress in the extraction roadway. Finally, based on this, the surrounding rock failure characteristics under different layout configurations of the extraction roadway are analyzed, providing a theoretical basis for the layout choice of the extraction roadway in this coal mine and offering references for similar engineering projects in other mines.

2. Analysis of Mine Pressure on the Floor of Deep-buried Coal Seam under Mining Induced Stress

2.1 Construction of the Support Stress Model for Deep-buried Coal Seams under Mining-Induced Stress

During the mining process of a coal seam, the formation of a goaf leads to the redistribution of the overlying rock load onto the surrounding coal and rock mass, thereby establishing a support pressure zone around the goaf [13]. For simplification in calculations, it is assumed that the support pressure adopts the configuration illustrated in Figure 1. A coordinate system is defined with its origin (point O) positioned at the boundary between the goaf and the intact coal seam. In this study, the floor is idealized as an isotropic semi-infinite body, and the abutment pressure is described using a piecewise linear profile. The coal–rock parameters within the analysis domain are assumed to remain stable during deformation, enabling the model to capture the dominant features of abutment-pressure transmission under deep, well-stratified geological conditions. While the semi-infinite body formulation effectively reflects the macroscopic attenuation of floor stress at a depth of ~730 m, its homogeneity and continuity assumptions may be influenced by lithological heterogeneity, bedding planes, and joint development, resulting in localized deviations. To address these factors, FLAC3D simulations and field monitoring were used to supplement and verify the theoretical model. The consistent results confirm that, within its applicable range, the semi-infinite body approach provides a reliable basis for engineering-scale floor stress analysis. These assumptions aim to extract the dominant features of abutment pressure transmission, and their applicability is primarily oriented toward deep, well-stratified engineering settings.

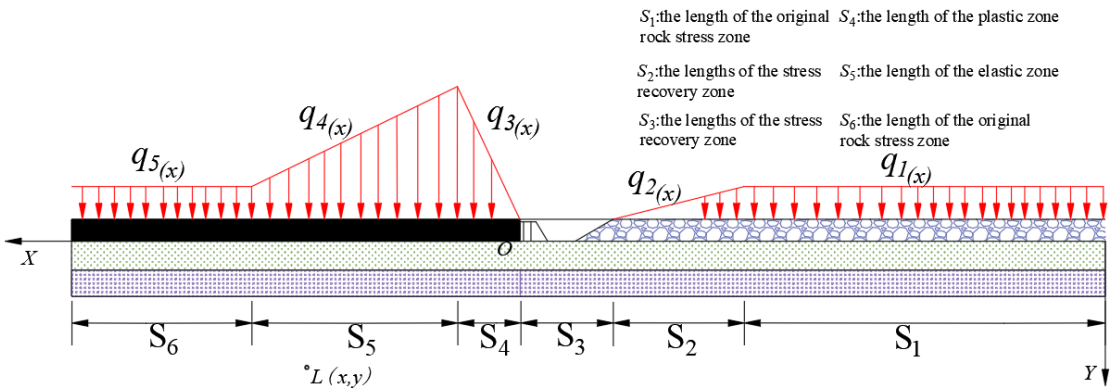

Figure 1: Simplified mechanical model of the stressed rock strata in the mined floor

2.2 Stress Calculation of Deep-Buried Coal Seam Floor Under Mining Activities

The support pressure in front of and behind the working face shifts continuously as mining progresses. To simplify calculations, it is assumed that both the distribution and magnitude of the support pressure remain constant, with its relative position to the *Y*-axis unchanged. The advancement of the working face can be regarded as a horizontal movement of the support pressure along the *OX* direction. Assuming that the working face moves positively along the *X*-axis by a distance of *x* and positively along the *Y*-axis by a distance of *y* to reach point L, we denote the coordinates of point *L* as *L*(*x*,*y*). A small segment is considered to be located to the left of coordinate origin *O*, where we analyze the force acting on this segment as a concentrated force.

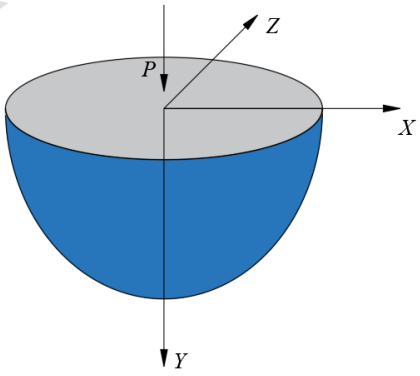

Figure 2: Computational Model for Semi-Infinite Body

Assuming the coal seam is modeled as a half-infinite medium, as illustrated in Figure 2 [22], the stress at any point *L*(*x*,*y*) induced by the infinitesimal segment $d\lambda$ can be determined based on the principles of elasticity theory:

$$\begin{cases} \sigma_x = -\dfrac{2}{\pi}\displaystyle\int_{-\infty}^{\infty} \dfrac{q(\lambda)\,\mathrm{y}^3\,d\lambda}{\left[y^2+(x-\lambda)^2\right]^2} \\ \sigma_y = -\dfrac{2}{\pi}\displaystyle\int_{-\infty}^{\infty} \dfrac{q(\lambda)\,\mathrm{y}(x-\lambda)^2\,d\lambda}{\left[y^2+(x-\lambda)^2\right]^2} \\ \tau_{xy} = -\dfrac{2}{\pi}\displaystyle\int_{-\infty}^{\infty} \dfrac{q(\lambda)\,\mathrm{y}^2(x-\lambda)\,d\lambda}{\left[y^2+(x-\lambda)^2\right]^2} \end{cases} \tag{1}$$

Based on the pressure distribution observed in the simplified mechanical model, it can be inferred that:

$$\begin{cases} q_1(x) = \gamma H\left(-\infty < x \le -S_3 - S_2\right) \\ q_2(x) = -\dfrac{S_3 + x}{S_2}\gamma H\left(-S_3 - S_2 \le x \le -S_3\right) \\ q_3(x) = -\dfrac{k\gamma H}{S_4}x\left(0 \le x \le S_4\right) \\ q_4(x) = \dfrac{(1-k)(x-S_4)}{S_5}\gamma H + k\gamma H\left(S_4 \le x \le S_4 + S_5\right) \\ q_5(x) = \gamma H\left(S_4 + S_5 \le x \le +\infty\right) \end{cases} \tag{2}$$

Where: γ represents the average unit weight of the rock strata; k represents the lateral support pressure concentration factor; H represents the burial depth; S_1 and S_6 represent the length of the original rock stress zone; S_2 and S_3 represent the lengths of the stress recovery zone; S_4 represents the length of the plastic zone; S_5 represents the length of the elastic zone.

By substituting $q_i(x)$ into equation (1) and calculating the stress at point $L(x,y)$ under its effect, the vertical stress σ_y, horizontal stress σ_x, and shear stress τ_{xy} induced by the supporting pressure above the coal seam at any point can be determined by summing the respective stress components.

$$\begin{cases} \sigma_x = \sigma_{x1} + \sigma_{x2} + \sigma_{x3} + \sigma_{x4} + \sigma_{x5} \\ \sigma_y = \sigma_{y1} + \sigma_{y2} + \sigma_{y3} + \sigma_{y4} + \sigma_{y5} \\ \tau_{xy} = \tau_{xy1} + \tau_{xy2} + \tau_{xy3} + \tau_{xy4} + \tau_{xy5} \end{cases} \tag{3}$$

After substituting the values into equation (3) and conducting the necessary calculations, the expression for the vertical stress σ_y is derived as follows:

$$\sigma_x = \frac{k\gamma Hy}{\pi S_4}\ln\frac{(S_4-x)^2+y^2}{x^2+y^2}+\frac{k\gamma Hx}{\pi S_4}\left(\arctan\frac{S_4-x}{y}+\arctan\frac{x}{y}\right)+\frac{k\gamma Hy(x-S_4)}{\pi\left[(S_4-x)^2+y^2\right]}+\frac{k\gamma Hy(S_4+S_5-x)}{\pi\left[(S_4+S_5-x)^2+y^2\right]}+$$
$$\frac{\left[(1-k)(x-S_4)+kS_5\right]\gamma H}{\pi S_5}\left(\arctan\frac{S_4+S_5-x}{y}-\arctan\frac{S_4-x}{y}\right)-\frac{\gamma Hy}{\pi S_2}\ln\frac{(S_3+x)^2+y^2}{(S_2+S_3+x)^2+y^2}+$$
$$\frac{(1-k)\gamma Hy}{\pi S_5}\ln\frac{(S_4+S_5-x)^2+y^2}{(S_4-x)^2+y^2}+\frac{(1-k)\gamma Hy^3}{\pi S_5}\left[\frac{1}{(S_4+S_5-x)^2+y^2}-\frac{1}{(S_4-x)^2+y^2}\right]+\gamma H-$$
$$\frac{(S_3+x)\gamma H}{\pi S_2}\left(\arctan\frac{S_2+S_3+x}{y}-\arctan\frac{S_3+x}{y}\right)-\frac{\gamma Hy^3}{\pi S_2}\left[\frac{1}{(S_3+x)^2+y^2}-\frac{1}{(S_2+S_3+x)^2+y^2}\right]-$$
$$\frac{(S_3+x)\gamma Hy}{\pi S_2}\left[\frac{S_3+x}{(S_3+x)^2+y^2}-\frac{S_2+S_3+x}{(S_2+S_3+x)^2+y^2}\right]-\frac{\gamma H}{\pi}\arctan\frac{S_2+S_3+x}{y}+\frac{(S_2+S_3+x)\gamma Hy}{\pi\left[(S_2+S_3+x)^2+y^2\right]}-$$
$$\frac{\gamma Hy\left[(1-k)(x-S_4)+kS_5\right]}{\pi S_5}\left[\frac{S_4+S_5-x}{(S_4+S_5-x)^2+y^2}-\frac{S_4-x}{(S_4-x)^2+y^2}\right]-\frac{\gamma H}{\pi}\arctan\frac{S_4+S_5-x}{y} \tag{4}$$

The expression for the horizontal stress σ_x at the lower point L is as follows:

$$\sigma_y = \frac{k\gamma Hx}{\pi S_4}\left(\arctan\frac{S_4-x}{y}+\arctan\frac{x}{y}\right)+\frac{k\gamma Hy(S_4-x)}{\pi S_4\left[(S_4-x)^2+y^2\right]}-\frac{\gamma H}{\pi}\arctan\frac{S_2+S_3+x}{y}-$$
$$\frac{\gamma Hy(S_2+S_3+x)}{\pi\left[(S_2+S_3+x)^2+y^2\right]}+\frac{\left[(1-k)(x-S_4)+kS_5\right]\gamma H}{\pi S_5}\left(\arctan\frac{S_4+S_5-x}{y}-\arctan\frac{S_4-x}{y}\right)-$$
$$\frac{\gamma H}{\pi}\arctan\frac{S_4+S_5-x}{y}-\frac{\gamma Hy(S_4+S_5-x)}{\pi\left[(S_4+S_5-x)^2+y^2\right]}+\frac{\left[(1-k)(x-S_4)+kS_5\right]\gamma Hy}{\pi S_5}\left[\frac{S_4+S_5-x}{(S_4+S_5-x)^2+y^2}-\frac{S_4-x}{(S_4-x)^2+y^2}\right] \tag{5}$$
$$+\gamma H+\frac{(1-k)\gamma Hy^3}{\pi S_5}\left[\frac{1}{(S_4-x)^2+y^2}-\frac{1}{(S_4+S_5-x)^2+y^2}\right]-\frac{\gamma Hy^3}{\pi S_2}\left[\frac{1}{(S_2+S_3+x)^2+y^2}-\frac{1}{(S_3+x)^2+y^2}\right]-$$
$$\frac{(S_3+x)\gamma Hy}{\pi S_2}\left[\frac{S_2+S_3+x}{(S_2+S_3+x)^2+y^2}-\frac{S_3+x}{(S_3+x)^2+y^2}\right]-\frac{(S_3+x)\gamma H}{\pi S_2}\left(\arctan\frac{S_2+S_3+x}{y}-\arctan\frac{S_3+x}{y}\right)$$

The expression for the shear stress at the bottom L point, denoted as τ_{xy}, is as follows:

$$\tau_{xy} = \frac{k\gamma Hx}{\pi S_4}\left(\arctan\frac{S_4-x}{y}+\arctan\frac{x}{y}\right)+\frac{\gamma Hy^2}{\pi}\left[\frac{1}{(S_4+S_5-x)^2+y^2}-\frac{k}{(S_4-x)^2+y^2}\right]+\frac{k\gamma Hy^2}{\pi\left[(S_4-x)^2+y^2\right]}+$$
$$\frac{(1-k)\gamma Hy}{\pi S_5}\left(\arctan\frac{S_4-x}{y}-\arctan\frac{S_4+S_5-x}{y}\right)-\frac{\gamma Hy}{\pi S_2}\left(\arctan\frac{S_3+x}{y}-\arctan\frac{S_2+S_3+x}{y}\right)-\frac{\gamma Hy^2}{\pi\left[(S_4+S_5-x)^2+y^2\right]} \tag{6}$$

From equations (4), (5), and (6), it can be observed that the vertical stress, horizontal stress, and shear stress at any point L on the bottom are influenced by both the vertical distance y and the horizontal distance x from the coal seam floor. These stresses can be quantified using the provided formulas, thereby facilitating an analysis of the stress field distribution beneath the floor as affected by mining activities.

3 Stress Field Distribution in the Coal Seam Bottom Under Mining Influence

3.1 Analytical Solution of Stress Field in Coal Seam Bottom

Based on the analysis and calculations of the working face conditions at a coal mine in Shanxi, the values of the parameters are as follows: γ =25KN/m^3, H =730m, k =2.5, S_2 =51m, S_3 =10m, S_4 =10m, S_5 =40m. Based on equation (4), the relationship curves illustrating the vertical stress, distance from the floor, and advancing distance of the working face were generated using MATLAB. Furthermore, the spatial distribution of stress beneath the working face floor was visualized as well.

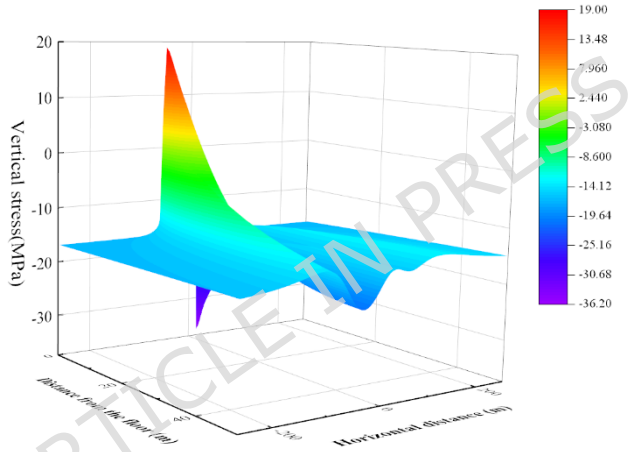

Figure 3: Vertical Stress Distribution on the Foundation Plate

The variation curves of vertical stress with horizontal distance at various depths below the floor are illustrated in Figure 4. As the working face advances, the vertical stress at different depths exhibits a similar trend with respect to horizontal distance. Notable stress concentration is observed near the working face, where peak stresses reach approximately 37.25 MPa at the coal pillars flanking both sides of the working face. At the center of the working face, stress levels stabilize, averaging around 16 MPa, which is comparable to the original rock stress measured at 14.58 MPa. As one moves further away from the coal pillar horizontally, vertical stress tends to revert towards its original rock value. Additionally, as depth increases from the floor level, there is a general decline in vertical stress; however, this rate of decrease significantly diminishes beyond a depth of 5 meters. This distribution pattern of stress underscores the spatial attenuation characteristics associated with mining-induced disturbances within the floor rock mass.

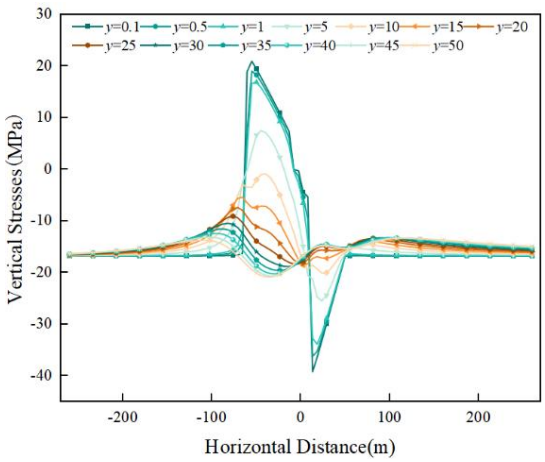

Figure 4: Vertical stress change curves at different horizontal distances below the foundation

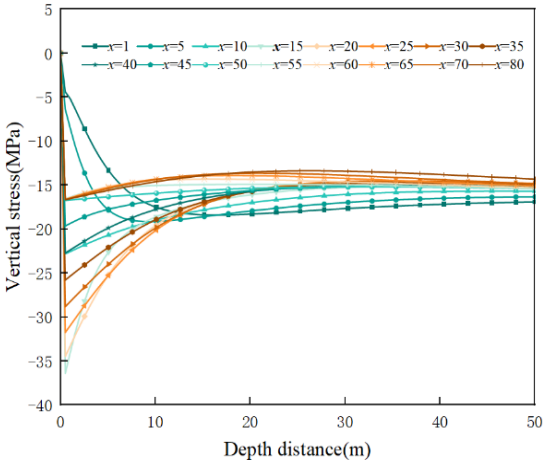

Figure 5: Vertical stress change curves at different depth distances below the foundation

The variation curve of vertical stress with floor depth at different horizontal distances is illustrated in Figure 5. The vertical stress rapidly reaches its peak at (y=0), and this peak stress demonstrates a trend characterized by an initial increase followed by a subsequent decrease as the horizontal distance (x) increases. This gradual decline in peak stress suggests that, as the working face advances, the floor stress progressively diffuses into deeper strata. Ultimately, with further increases in depth (y), the vertical stress stabilizes within a range of 15 MPa to 17 MPa, which approximates the original rock stress. This behavior highlights the capacity of deep surrounding rock to self-adjust and mitigate the effects of mining-induced disturbances.

3.2 Simulation of Bottom Coal Seam Stresses Under Mining Influence

Mining-induced effects result in the redistribution of stress on the floor of the working face, with stress shifting from the overlying rock layers to the surrounding areas of the mining site. This phenomenon can lead to stress concentration in localized regions of both the floor and surrounding rock, potentially causing shear failure, bending deformation, or tensile fracturing within the floor rock. Such conditions may even compromise the stability of adjacent rock formations. Consequently, these factors significantly impact the stability of roadway floors in active mining faces. To investigate the characteristics of stress and plastic zone distribution in response to mining-induced effects, FLAC3D is employed to elucidate stress field distribution, complemented by an analytical solution for validation purposes.

3.2.1 Numerical Model Setup

The bottom extraction roadway in a coal mine located in Shanxi serves the overlying working face and is utilized for the pre-drainage of regional gas. Consequently, it is essential

to advance the roadway prior to the extraction process. However, during the extraction period, floor stress significantly impacts the stability of the bottom extraction roadway. Therefore, investigating the stress distribution characteristics of the coal seam floor during mining operations is crucial for evaluating the stability of this roadway. The parameter sensitivity analysis indicates that the strain-softening model, after accounting for the degradation of surrounding rock strength, predicts a plastic zone that is approximately 15%–25% larger than that obtained using the Mohr–Coulomb model, while the estimated peak stress is slightly reduced by about 5%–10%. Although quantitative differences exist between the two models in terms of plastic zone extent and peak stress, they remain highly consistent in the overall stress-field distribution pattern, locations of stress concentration, and the comparative assessment of different floor-drainage roadway layouts. These results demonstrate that the Mohr–Coulomb model can reliably capture the dominant stress characteristics under mining-induced disturbance, and its predictive trends align well with those of the more sophisticated model; thus, it provides a robust computational basis for scheme screening and comparative analysis in this study.

A numerical model with dimensions $520 \times 200 \times 100$ (length $\times$ width $\times$ height) was developed based on the stratigraphic conditions illustrated in Figure 6. Displacement constraints were imposed along the *x*-axis and *y*-axis as well as at the bottom boundary of the *z*-axis. A load of 14.18 MPa was applied to the top boundary of the *z*-axis. To simulate the impact of mining activities on stress distribution within the floor strata, a working face designated as 31018 was excavated along the *y*-axis for a length of 200 m.

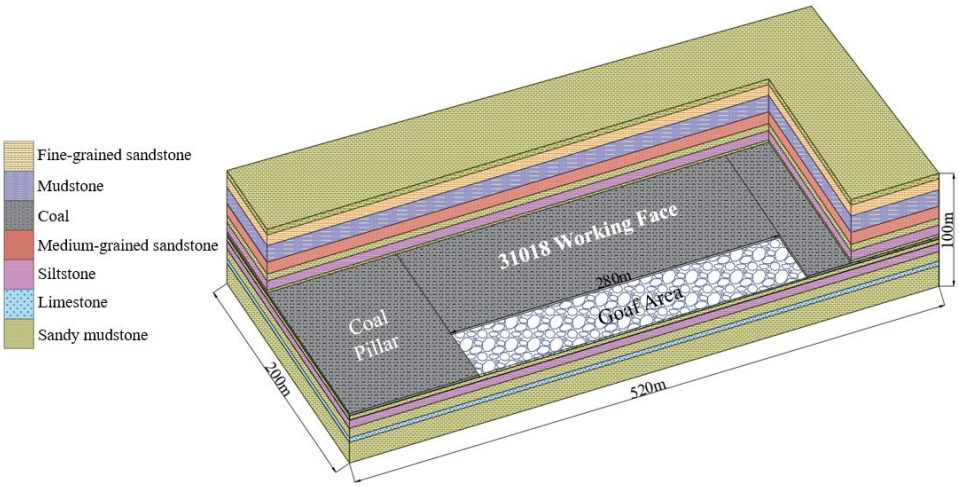

Figure 6: Numerical Computation Model

Based on field drilling data, The rock mass parameters were derived from a combination of laboratory tests, field back-analysis, and regional engineering data; the cohesion and internal friction angle were calibrated by inversion of monitored deformation, and the deep-seated parameters were taken from geological reports. Sensitivity analysis with ±20% variation in the key parameters shows that the peak stress changes by <10% and the extent of the plastic zone changes by <15%, indicating good stability of the parameter system. the selected parameters for the model are shown in Table 1.

Table 1: Numerical Model Rock Parameters Table

lithology	Density（kg/m^3）	Modulus of volume（GPa）	Shear modulus（GPa）	Cohesion（MPa）	Internal friction angle（°）	Tensile strength（MPa）
Coal	1640	2.67	2.02	2.15	30	2.12
Medium-grained sandstone	2650	3.16	1.95	3.68	38	2.65
Sandstone shale	2320	9.63	6.35	3.86	32	2.36
Fine-grained sandstone	2550	1.68	1.23	2.21	36	5.28
Shale	2200	5.00	3.00	1.52	30	1.56
Siltstone	2460	15.6	10.8	2.75	32	1.84
Limestone	2090	22.6	11.1	6.72	42	1.58

3.2.2 Stress Distribution Characteristics of the Working Face Floor

Based on the prior calculations and analysis of the stress distribution within the floor, this study aims to elucidate the stress distribution pattern at the working face floor and to identify an appropriate layer for the bottom extraction roadway. To achieve this, we monitored the supporting stress at various depths—specifically 5 m, 10 m, 15 m, 20 m, 25 m, and 30 m below the floor [22]. The results of this monitoring are presented in Figure 7.

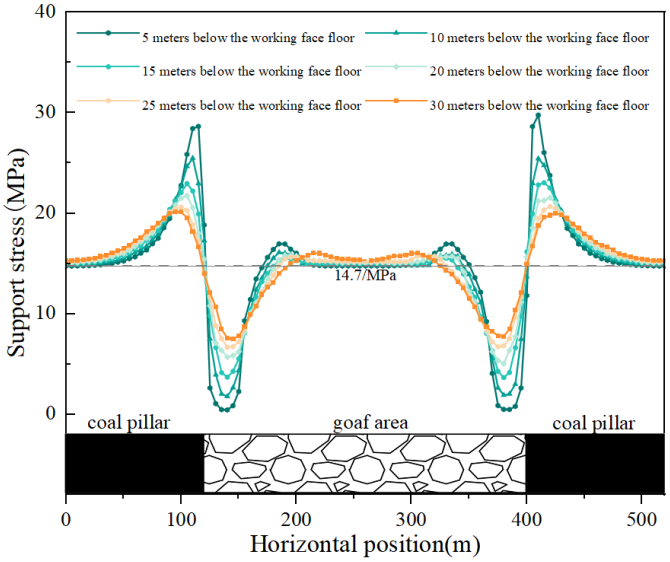

Figure 7: Stress map below the slab

The abutment stress at depths of 5m, 10m, 15m, 20m, 25m, and 30m below the working face floor was analyzed and is illustrated in Figure 7. The stress stabilizes near the coal wall at approximately 14.7 MPa, which is close to the in situ stress level. In the goaf area, the stress distribution exhibits an "M" shape pattern; notably, peak stresses diminish with increasing depth. Additionally, the degree of stress concentration decreases as one moves further away from the floor. The maximum peak stress occurs at a depth of 5m below the floor, reaching a value of 2.04 MPa; conversely, the minimum peak stress is recorded at a depth of 30m with a value of 1.43 MPa. The most rapid attenuation of peak stress takes place at a depth of 10m below the floor; beyond this point, there is a significant reduction in the rate of attenuation. Consequently, it can be preliminarily concluded that horizontal planes situated below a depth of 10m are identified as optimal for arrangement purposes.

The vertical stress variation curve with respect to horizontal distance at various depths below the floor, as illustrated in Figure 4, demonstrates that the vertical stress distribution pattern within the floor remains consistent across different depths as the working face progresses. Vertical stress tends to concentrate near the coal pillars flanking both sides of the working face, reaching peak values before stabilizing near the center of the working face, where it approximates in situ stress levels. Similarly, at locations further from the working face on either side, vertical stress also approaches in situ values. The observed discrepancy between these two measurements is 8.13%. This alignment between analytical and numerical solutions for coal seam floor stress substantiates the accuracy of our previously derived analytical model concerning the stress field of the coal seam floor. To avoid ambiguity in the

expression “overall consistency,” this study adopts quantitative criteria for verification: the error between the analytical and numerical solutions at the vertical stress peak is approximately 8–12%, the difference in stress attenuation depth is less than 10%, and the spatial distribution pattern of the stress field remains consistent. On this basis, the two approaches can be considered to exhibit good consistency at the engineering evaluation scale.

4. Optimization of the Bottom Extraction Roadway Location in Deep-Buried Coal Seams Under Mining Influence

4.1 Selection of the Bottom Extraction Roadway Layer

Based on the theory of the floor sliding line field, a model for coal seam floor failure has been established. The maximum depth of floor failure induced by mining activities at the working face is [23]:

$$h_{\max} = \frac{\cos^2\alpha}{\pi\gamma} \times \left[\frac{(k+1)\gamma H}{2} - P \right] \times \left[\beta \left(\cos\alpha - \frac{\sin\alpha}{\sin\varphi_0} \right) - \frac{\sin\beta}{\sin\varphi_0} \right] + \frac{C\cos\alpha}{\gamma\tan\varphi_0} + \frac{M}{\lambda - 1} \quad (7)$$

$$\beta = \arccos\left(\cos\alpha \sin\varphi_0 - \sin\alpha \right) \quad (8)$$

Where: $h_{\max}$ represents the maximum failure depth of the coal seam floor; γ represents the unit weight of the rock layer beneath the working face floor, which is taken as 2530 kg/m³; k represents the concentration factor of the advanced support pressure in the working face, which is taken as 1.5; α represents the dip angle of the coal seam in the direction of extraction, which is taken as 9°; H represents the mining depth of the coal seam, which is taken as 0.73 km; P represents the confining water pressure, which is taken as 5 MPa; φ_0 represents the average internal friction angle of the floor rock mass, which is taken as 40°; C represents the average cohesion of the coal seam floor, which is taken as 2.45 MPa; M represents the thickness of the coal seam, which is taken as 5 m; λ represents the collapse and bulking coefficient of the goaf roof, which is taken as 1.3.

Through calculations, it has been determined that the maximum failure depth of the floor during the extraction process at the 31018 working face is 16.51 m. In conjunction with prior analyses regarding the stress beneath the working face floor, it is recommended that the

bottom extraction roadway be situated at a depth of approximately 17 m below the coal seam floor. Building upon earlier studies concerning stress distribution and failure depths influenced by mining activities, and taking into account both the surrounding rock stress environment and the stability of the roadway itself, it has been decided to position the bottom extraction roadway at a horizontal plane located 17 m beneath the goaf floor.

Based on the established depth of the bottom extraction roadway, the roadway will experience varying degrees of stress disturbance depending on its position relative to the working face. Consequently, four layout schemes for the bottom extraction roadway have been designed [22]: ① The bottom extraction roadway is situated at the center of the working face. ② The bottom extraction roadway is located 30 m inward from the coal pillar boundary. ③ The bottom extraction roadway is positioned at the coal pillar boundary of the 31018 working face. ④ The bottom extraction roadway is placed at the center of the coal pillar, extending 30 m outward from its boundary. These four layout schemes are illustrated in Figure 8.

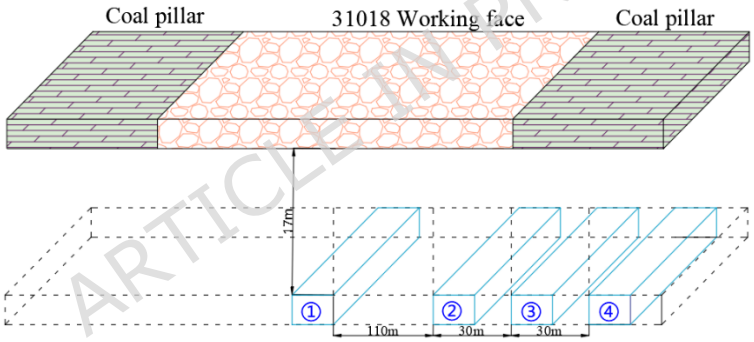

Figure 8: Mine shaft arrangement

4.2 Stress Distribution and Failure Characteristics of the Surrounding Rock in the Bottom Extraction Roadway

To enhance the comparability among the four layout schemes, a unified evaluation framework is adopted: (i) the peak vertical stress and the location of the concentration zone; (ii) the peak horizontal stress and its offset characteristics; (iii) the scale of the plastic zone and the failure mode; and (iv) the coupled stress–plasticity response of the roadway ribs and roof–floor. These indicators directly reflect the differences in overall roadway stability under mining-induced disturbance.Using the previously established numerical model, the bottom extraction roadway is positioned at a depth of 17 meters below the working face floor, and the 31018 working face is subsequently mined. The layout schemes for the bottom extraction

roadway are as follows: at the center of the working face; 30 meters inward from the coal pillar boundary; along the coal pillar boundary; and 30 meters outward from the coal pillar boundary. An analysis of stress distribution and surrounding rock failure characteristics for each of these four layout schemes is conducted.

4.2.1 Vertical Stresses in Deep-Set Bottom-Pulling Roadways

As the working face progresses, the vertical stress exerted on the surrounding rock of the roadway will gradually increase. When this stress becomes excessive, it can lead to compressive deformation of the surrounding rock. This phenomenon is particularly critical in areas where the surrounding rock layers are weak; an increase in vertical stress may result in squeezing of these rocks, ultimately causing cracking, subsidence, or deformation of both the floor and roof structures.

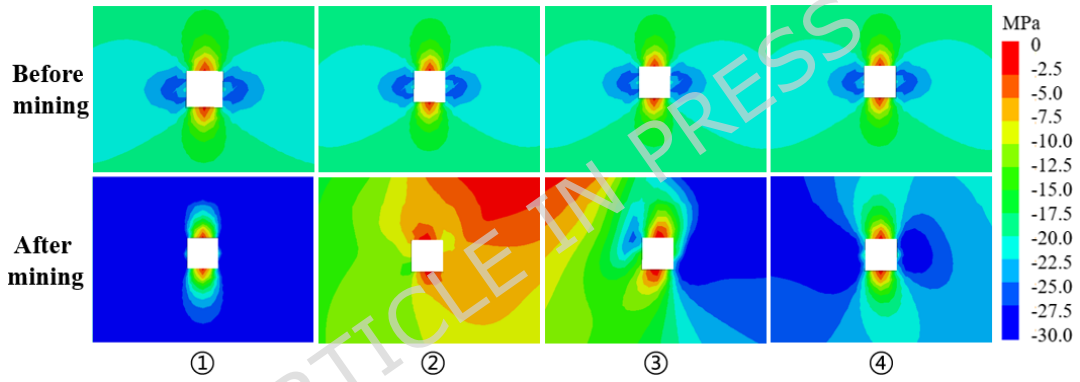

Figure 9: Distribution Map of Vertical Stress

As illustrated in Figure 9, prior to the mining of the working face, the vertical stress within the surrounding rock of the bottom extraction roadway demonstrates a symmetrical distribution. Stress concentration zones are identified on both sides of the roadway, with a peak stress value reaching approximately 21.17 MPa. In contrast, a stress relief zone is observed in the shallow regions of both the roof and floor, exhibiting a stress value around 1.25 MPa. This particular distribution of stress can be attributed to the equilibrium of forces acting on either side of the 31018 working face.

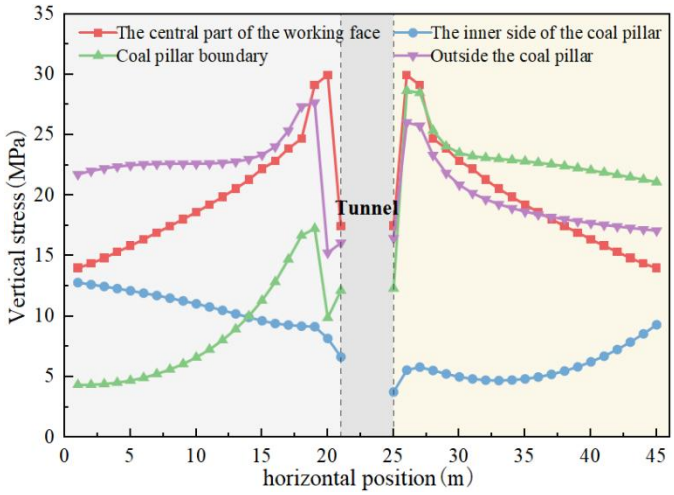

Figure 10 Vertical stress curves on the sides of the tunnel.

After the working face has been mined, only the vertical stress of the surrounding rock in the center of the working face displays a symmetrical distribution. Stress concentration is observed on both sides of the roadway, with a peak value reaching approximately 29.92 MPa, which represents an increase of 41.33% compared to pre-mining conditions. The shallow regions of both the roof and floor exhibit decompression zones characterized by stress values around 1.83 MPa. When the extraction roadway is offset within the coal pillar, decompression zones emerge in the shallow areas of both the roof and floor, with stress values approximately at 1.36 MPa. Stress concentration occurs on either side of the roadway as well, with peak values around 10.55 MPa—indicating a decrease of 50.17% relative to pre-mining conditions. When the extraction roadway is situated at the boundary of the coal pillar, decompression zones also develop in the shallow regions of both the roof and floor, exhibiting stress values around 1.62 MPa. The area of stress concentration on the right side of the roadway is considerably larger than that on the left side, with a noticeable shift in the position of this concentrated region. The peak stress observed on the left side measures approximately 17.26 MPa, reflecting an 18.47% reduction compared to pre-mining conditions, whereas the peak stress on the right side reaches about 28.65 MPa, indicating a significant increase of 35.33%. When the extraction roadway is positioned outside the coal pillar, the vertical stress distribution of both the roof and floor remains nearly identical. Stress concentration occurs on either side of the roadway; however, the regions of concentration vary. The peak stress on the left side reaches approximately 27.79 MPa, reflecting an increase of 31.27% compared to pre-mining conditions, while the peak stress on the right side is about 26.61 MPa, indicating a rise of 25.69%. These phenomena arise from lateral stress transfer downward following mining activities and are influenced by the relative offsets among three layout

configurations—within the coal pillar, at its boundary, and outside it—in relation to the center of the working face, thereby altering vertical stress distribution.

From Figure 9(b), it is clear that the vertical stress in the roadway is significantly reduced under the influence of mining activities when the roadway is positioned within the coal pillar, as opposed to the other three layout configurations. This phenomenon can be attributed to the fact that after excavation of the working face, the roof collapses and makes direct contact with the floor in most areas. However, in this particular layout, at the offset location, there is incomplete contact between the collapsed roof and floor, which disrupts stress transmission.

4.2.2 Horizontal Stress in Extraction Roadway of Deeply Buried Coal Seam

Horizontal stress typically induces shear failure in the surrounding rock along fault planes or weak zones. Under the influence of mining-induced stress, the horizontal stress acting on the surrounding rock can result in relative sliding between rock layers. This phenomenon is particularly pronounced in regions characterized by deep burial and high stress, where horizontal stress may serve as a primary catalyst for the cracking and sliding of the roadway's surrounding rock.

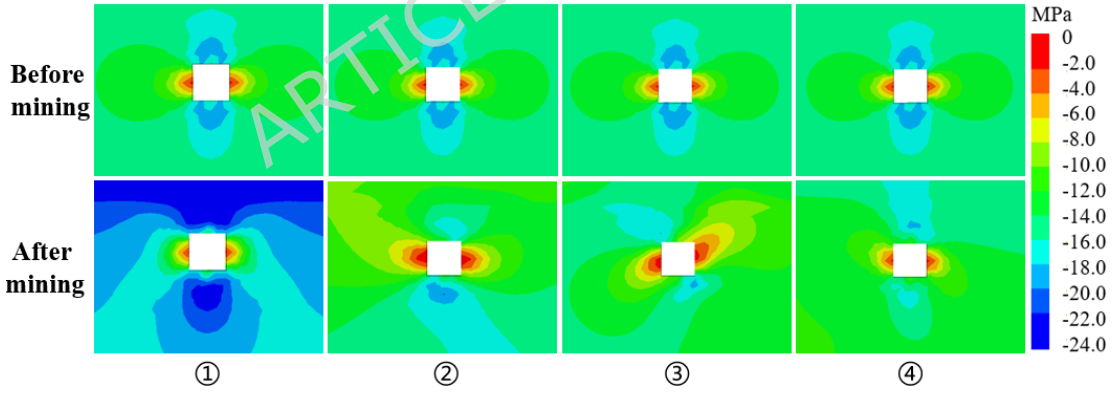

Figure 11: Distribution Map of Horizontal stresses

As illustrated in Figure 11, when the working face remains unmined, both the horizontal and vertical stresses acting on the roadway display symmetrical distributions. However, the locations of stress concentration and relief zones are distinct. Stress concentration is observed at both the roof and floor of the roadway, reaching a peak value of approximately 21.62 MPa. In contrast, stress relief zones manifest along both sides of the roadway, exhibiting a stress value of around 1.35 MPa. This phenomenon can be attributed to the symmetrical overall force distribution present at the 31018 working face.

After the working face has been mined, the horizontal stress distribution within the roadway remains symmetric when it is positioned at the center of the working face bottom plate. The stress concentration in both the top and bottom plates reaches a peak value of approximately 23.92 MPa, representing an increase of 10.64% compared to pre-mining conditions. An unloading zone emerges on both sides of the roadway, exhibiting stress values around 2.22 MPa. When the roadway is offset within the coal pillar, the peak stress in the top plate measures approximately 17.45 MPa, reflecting a decrease of 19.29% relative to pre-mining conditions; conversely, the peak stress in the bottom plate rises to about 23.13 MPa, indicating an increase of 6.98%. The unloading zones on either side of this roadway exhibit a reduced stress value of approximately 0.68 MPa. For roadways situated at the boundary of coal pillars, there is a counterclockwise shift in both top and bottom plate stress concentration zones toward the shoulder of the roadway. The peak stress recorded is about 22.35 MPa, which signifies an increase of 3.38% compared to pre-mining conditions. Similarly, unloading zones on either side also shift alongside these areas with corresponding stress values around 1.51 MPa. In instances where roadways are located outside coal pillars, symmetry largely persists within unloading zones on both sides with approximate stress values around 1.66 MPa; however, alterations occur within top and bottom plate stress concentration zones as well as their respective peaks: specifically, peak stresses for these plates measure roughly at 19.37 MPa (indicating a decrease by 10.41%) for topside and about 17.59 MPa (reflecting an reduction by18 .62%) for underside stresses respectively. This observation suggests that relocating roadways concerning coal pillars significantly influences horizontal stress distribution patterns—impacting not only areas experiencing heightened concentrations but also those undergoing unloading effects.

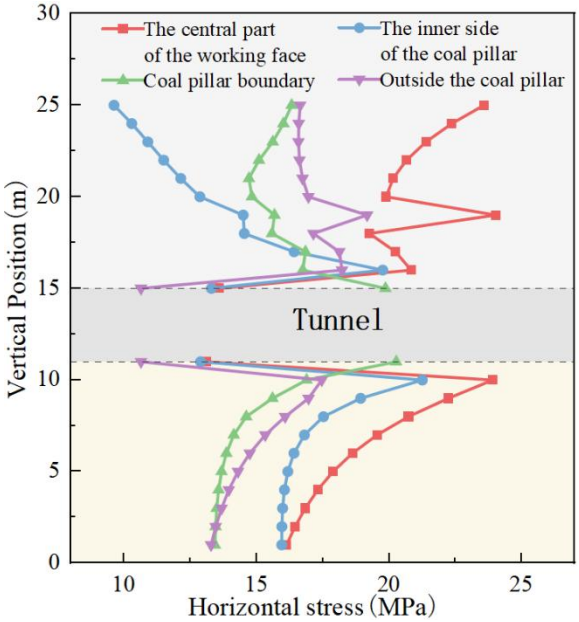

Figure 12 Horizontal Stress Curves of Roof and Floor of the tunnel

Under the influence of mining-induced stress, the roadway situated at the center of the working face exhibits a symmetric distribution of horizontal stress, with the maximum stress peak reaching 23.92 MPa. In contrast, the other three placement configurations demonstrate deviations from this central position, resulting in continuous lateral pressure transmission that alters the horizontal stress distribution within the roadway. The lowest peak horizontal stress recorded is 19.37 MPa, which occurs when the roadway is positioned outside of the coal pillar.

4.2.3 Characteristics of Rock Damage in Deep-Buried Coal Seam Extraction Roadway

The failure characteristics of the surrounding rock are primarily indicated by the plastic zone. As this plastic zone expands, the strength of the surrounding rock diminishes, necessitating that the support structure endure increased pressure—particularly in regions characterized by deep burial and high stress. Under such conditions, failures within the plastic zone can exacerbate sliding or collapse of the surrounding rock mass.

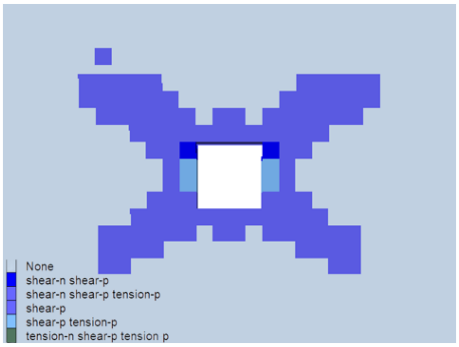

(a) The central part of the working face

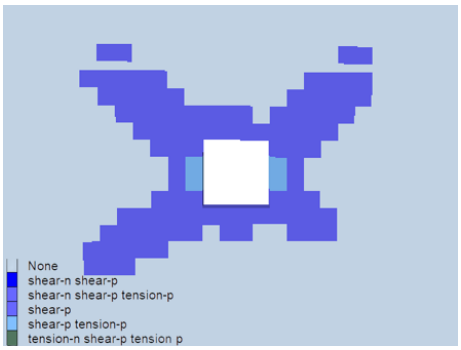

(b) The inner side of the coal pillar.

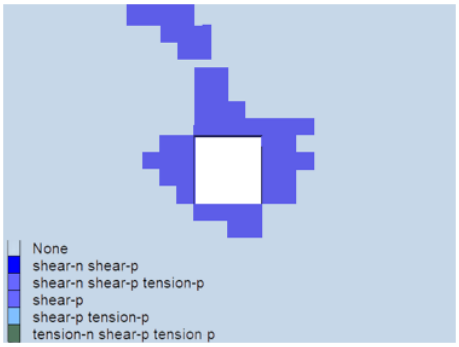

(c) Pillar boundaries

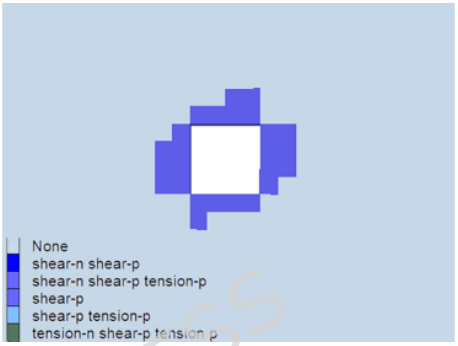

(d) Outside the coal pillar

Figure 13: shows the extent of rock damage in the tunnel surroundings.

Based on the four layout schemes—central position, in-shifted coal pillar, coal pillar boundary, and out-shifted coal pillar—simulations illustrating the failure characteristics of the surrounding rock in roadways following working face excavation are presented in Figure 13. In Figure 13(a), when the roadway is positioned centrally relative to the working face, the plastic zone displays a butterfly-shaped distribution. The maximum depth of damage to the bottom plate reaches a peak of 4 meters, while the plastic zone above the top plate also extends to 4 meters. The predominant mode of failure observed in the surrounding rock within this roadway is shear failure. In Figure 13(b), with an in-shifted roadway adjacent to the coal pillar, a similar butterfly-like distribution of plastic zones is noted. The maximum damage depth at the bottom plate again reaches 4 meters; however, there is a discontinuity observed in surrounding rock failure above the top plate. This phenomenon can be attributed to a limestone layer that is 0.5 meters thick and possesses greater strength, thereby inhibiting further extension of the plastic zone. In Figure 13(c), where the roadway aligns with the boundary of a coal pillar, we observe that maximum damage depth at the bottom plate measures up to 2 meters while extending up to 4 meters at its top plate. In scenarios devoid of limestone layers, it would be expected for both plastic zones (top and bottom plates) to connect within areas designated as gob. Figure 13(d) illustrates conditions where an

out-shifted roadway exists alongside a coal pillar; here, we find that maximum damage depth at both plates remains relatively modest at approximately 2 meters. The overall range of plastic failure affecting surrounding rock appears limited due primarily to reduced mining-induced stress experienced by roadways situated outside gob areas when shifted away from coal pillars.

4.3 Optimal Location Selection of Deep-buried Coal Seam Bottom-withdrawal Roadway Under Mining Impact

The positioning of the extraction roadway significantly influences the stability of the surrounding rock. Arranging the roadway at various locations beneath the working face leads to markedly different stress environments due to mining-induced effects, with the ultimate failure range of the surrounding rock being dictated by its most adverse stress environment. In deep and high-stress regions, an increase in the failure range of surrounding rock can result in uneven deformation within adjacent strata, thereby affecting both the bearing capacity and stability of the roadway. By integrating "butterfly-shaped plastic zone theory" with numerical simulation analysis, it becomes evident that when determining the position of the extraction roadway, it is essential to avoid situating it directly beneath the working face [22]. This strategy mitigates stress concentration effects arising from mining activities. Ideally, the extraction roadway should be positioned away from coal pillars, where both plastic failure zones in surrounding rock are minimized and damage depth to bottom plates is reduced. Furthermore, maximizing distance between top plate plastic zones and those associated with bottom plates at working faces enhances overall stability by lessening impacts from mining-induced stresses on roadway integrity. Engineering case analyses involving different combinations of burial depth and lithology show that the offset layout of the floor gas-drainage roadway remains consistently effective under a wide range of geological conditions. Although increasing burial depth elevates the floor stress level, the “M-shaped” pattern of mining-induced stress concentration and the location of the high-disturbance zone exhibit only minor variation; lithological differences between hard and weak strata primarily affect the scale of the plastic zone, with limited influence on the form of stress concentration. Overall, the results indicate that the key control on floor stress is governed by the spatial structure of the coal-pillar–gob system rather than burial depth or the strength of a single rock layer. The layout principles proposed in this study are thus applicable to deep, high-stress, and weak-surrounding-rock conditions, providing a transferable and replicable technical pathway and engineering reference for optimizing floor-drainage roadway design.

From the perspective of gas drainage, positioning the extraction roadway out-shifted from the coal pillar allows for its placement closer to the upper pre-excavated roadway. The 30 m offset layout significantly reduces the plastic zone around the roadway, maintains separation between the floor and gob plastic zones, and prevents the formation of a continuous failure chain. The peak stress attenuates laterally along the coal-pillar–gob boundary, and the resulting more uniform stress distribution effectively suppresses shear slip and localized fracturing. This optimization not only enhances gas drainage efficiency and reduces drilling and construction risks, but also decreases support investment and maintenance by approximately 10–20%, yielding about 8–15% savings in lifecycle cost and demonstrating both engineering–economic and mechanical advantages.This configuration effectively reduces the distance required for gas extraction, thereby enhancing the efficiency of gas drainage. In terms of roadway stability, situating the extraction roadway away from the coal pillar minimizes the failure range of surrounding rock. This significantly lowers maintenance costs associated with roadways and extends their service life. Consequently, taking into account both gas drainage efficiency and minimizing damage to surrounding rock under mining-induced stresses, it is determined that the optimal location for the extraction roadway in this coal mine is 17 meters below the bottom of the working face. It should be aligned in parallel with the working face and shifted 30 meters away from the coal pillar. This layout effectively balances gas extraction needs with roadway stability considerations.

5. On-site monitoring verification

5.1 Geological Overview and Support Forms

The 31018 working face at Shanxi Ping Shan Coal Mine is responsible for the extraction of the No. 3 coal seam, which is located in the lower section of the Shanxi Formation and positioned within the western wing of the mining area. This coal seam exhibits a relatively thin profile, with an average thickness of approximately 5 meters, and is classified as stable and mineable throughout the region. Based on drilling data from the mine, it has been determined that the average burial depth of the No. 3 coal seam is 730 meters; details regarding the lithology of both the roof and floor are illustrated in Figure 14. The specific support scheme for the extraction roadway associated with the 31018 working face is outlined as follows:

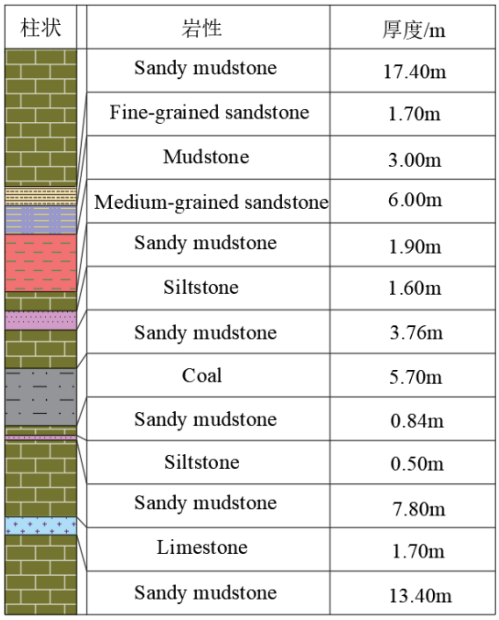

柱状	岩性	厚度/m
	Sandy mudstone	17.40m
	Fine-grained sandstone	1.70m
	Mudstone	3.00m
	Medium-grained sandstone	6.00m
	Sandy mudstone	1.90m
	Siltstone	1.60m
	Sandy mudstone	3.76m
	Coal	5.70m
	Sandy mudstone	0.84m
	Siltstone	0.50m
	Sandy mudstone	7.80m
	Limestone	1.70m
	Sandy mudstone	13.40m

Figure 14 Combined Column Chart of Coal (Rock) Layers

The roof support system employs a combined "bolt and cable" support method. Φ22mm×2600mm bolts are installed with 7 bolts per row, spaced 800mm apart, and the distance between rows is maintained at 1000mm. The bolts are positioned 200mm from the sidewalls. The cable spacing is set at 2000mm, featuring 5 cables per row that are spaced 1200mm apart; similarly, the distance from the cables to the sidewalls is also 200mm. For sidewall support, Φ22mm×2600mm bolts are utilized, arranged with 5 bolts per row and spaced 800mm apart. The interval between rows remains consistent at 1000mm. Additionally, these bolts are strategically placed at a distance of 300mm from both the roof and floor of the roadway.

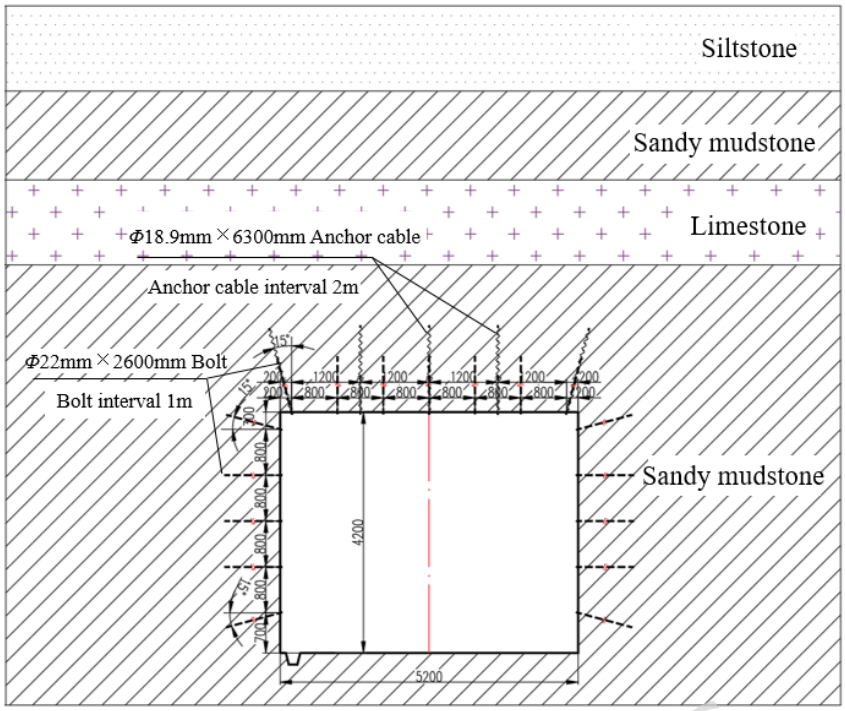

Figure 15 the support scheme for the roadway section

5.2 Excavation Disturbed Zone Range Test

In addition, during the mining operations at the 31018 working face, ultrasonic testing and borehole inspections utilizing a borehole viewing instrument were conducted to analyze the deformation of the roadway. Measurement points were strategically selected at positions 315m, 320m, and 325m along the Extraction Roadway (31018). The results of these assessments are illustrated in Figure 16. The borehole inspection primarily concentrated on the roof and shoulder areas of the roadway to evaluate the extent of surrounding rock failure. The findings from this inspection are presented in Figure 17.

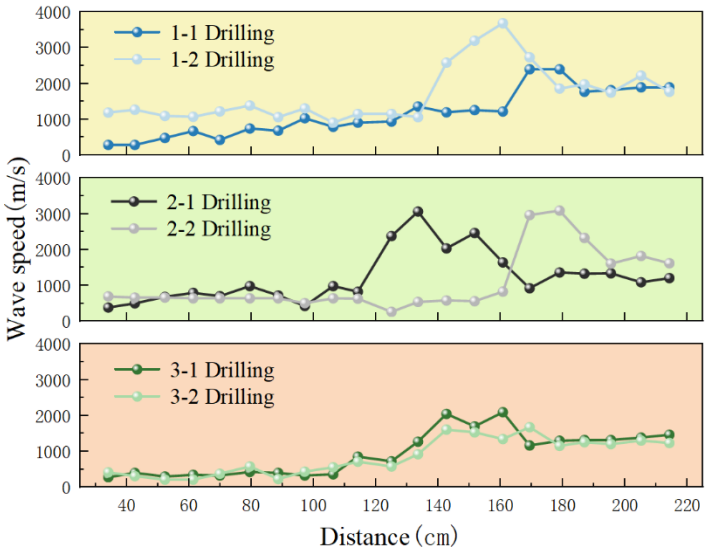

Figure 16 The drilling data for the bottom-up drift

Figure 16 shows the drilling data for the Extraction Roadway. For the 1-1 drilling point at the 31018 working face, the ultrasonic wave velocity fluctuates between 1400 m/s and 1800 m/s, with an average of 1600 m/s in the range of 0-1.3 m. The low wave velocity indicates that this area is a fractured zone. From 1.3 to 1.7 m, the ultrasonic wave velocity increases significantly, ranging from 1800 m/s to 2500 m/s, with an average of 2150 m/s, indicating a stress concentration in this plastic zone. Beyond 1.7 m, the wave velocity ranges from 2100 m/s to 2300 m/s, with an average of 2200 m/s, indicating that the surrounding rock is in the elastic region. Based on this, it can be concluded that the loosened zone around the roadway at drilling point 1-1 of the 31018 working face extends to 1.7 m. For the 1-2 drilling point, the ultrasonic wave velocity fluctuates between 1700 m/s and 2200 m/s, with an average of 1950 m/s in the range of 0-1.25 m, indicating that this area is also a fractured zone. From 1.25 to 1.65 m, the wave velocity significantly increases, ranging from 2500 m/s to 3700 m/s, with an average of 3100 m/s, suggesting stress concentration and a plastic zone in the surrounding rock. Beyond 1.65 m, the wave velocity ranges from 2500 m/s to 2700 m/s, with an average of 2600 m/s, indicating the elastic region. Therefore, the loosened zone around the roadway at drilling point 1-2 of the 31018 working face extends to 1.65 m.

Similarly, at drilling point 2-1, the loosened zone surrounding the roadway extends to a depth of 1.55 m; at drilling point 2-2, this zone reaches a depth of 1.8 m; at drilling point 3-1, it extends to 1.6 m; and at drilling point 3-2, the loosened zone measures approximately 1.7 m in depth. Based on the aforementioned analysis, it can be concluded that the fractured zone of the Extraction Roadway extends roughly to a distance of 1.17 m, while the plastic zone ranges from 1.17 m to 1.67 m. Furthermore, the radius of the loosened zone is estimated to be approximately 1.7 m.

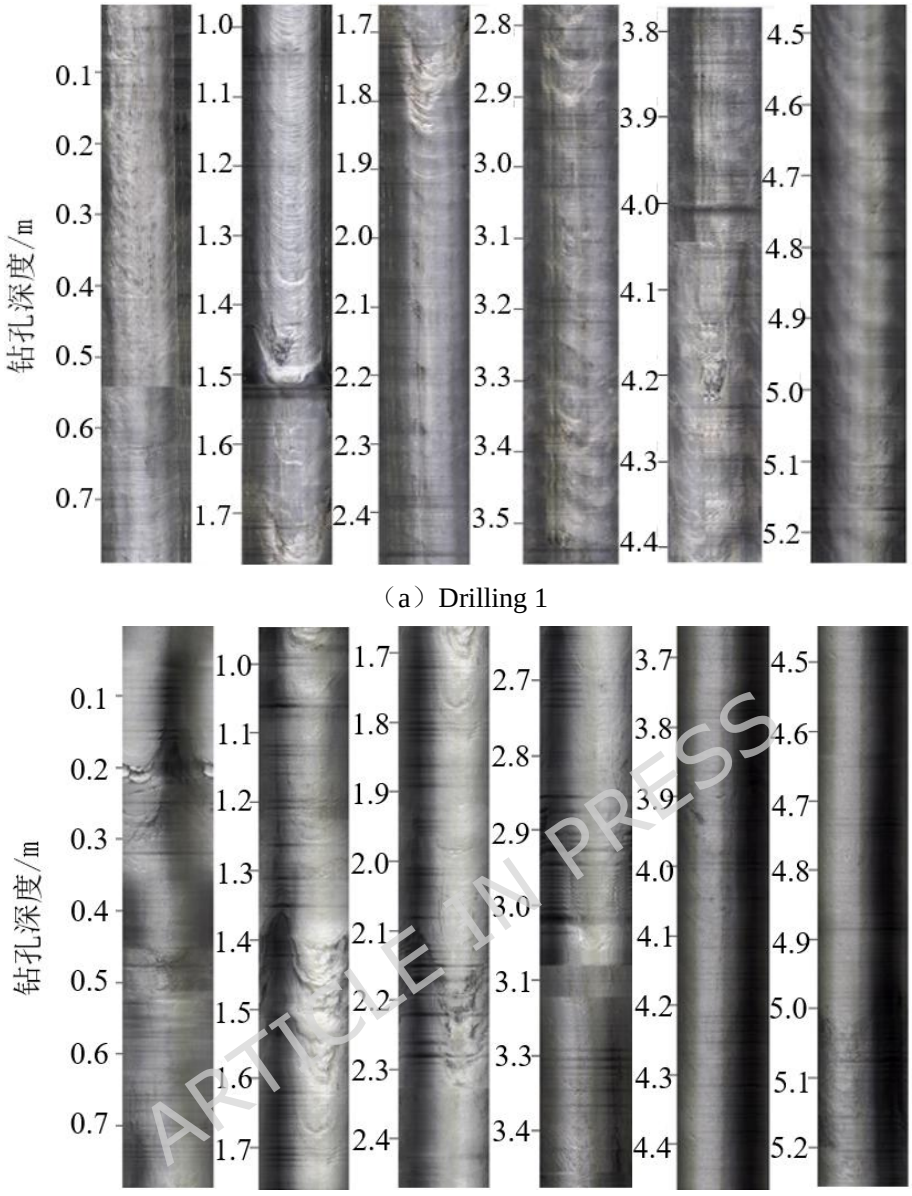

（a）Drilling 1

（b）Drilling 2

Figure 17: Drilling borehole view

Figure 17 illustrates the borehole inspection diagram. In the rock mass from 0 to 1.4 meters, circumferential cracks are frequently observed, indicating that the integrity of the surrounding rock in this section is relatively compromised. Between 1.4 and 1.9 meters, only a few circumferential cracks are detected, suggesting that the integrity of the surrounding rock in this segment is moderate. In the rock mass extending from 1.9 to 9 meters, there are virtually no visible cracks or damage, signifying that the integrity of the surrounding rock in this area is comparatively good. Based on a comprehensive analysis of both fracture range and crack development within the surrounding rock, it can be concluded that the maximum

fracture range identified in the borehole measures at 1.9 meters. This version retains clarity and detail essential for an academic context while enhancing overall flow and readability.

5.3 Roadway Displacement Monitoring

To gain a deeper understanding of the stability of the surrounding rock in the roadway, we monitored the deformation of the top and bottom plates, as well as both sides of the roadway. The surface displacement monitoring curves are presented in Figure 18. During the initial 15 days of monitoring, significant deformation was observed in the surrounding rock, characterized by rapid increases in displacement. The maximum deformation rates recorded were 10 mm/day for the bottom plate, 13 mm/day for the top plate, and 7 mm/day for both sides. From days 15 to 40, there was a transition to a phase of slow growth in deformation; during this period, all measured deformation rates—top and bottom plates as well as both sides—decreased to below 5 mm/day. After approximately 45 days of monitoring, stabilization of surrounding rock deformation was noted. The final recorded values indicated deformations of 262 mm for the top plate, 227 mm for the bottom plate, and 157 mm for both sides. Overall, it can be concluded that the stability of the surrounding rock is satisfactory since no significant deformations occurred within the roadway cross-section. The monitoring points were arranged in segments at the key stress-bearing locations of the roadway, and the borehole depths covered 0–9 m, enabling comprehensive characterization of the fractured, plastic, and elastic zones. The monitoring frequency was dynamically adjusted with the advance of the working face to ensure effective capture of fracture propagation during mining-sensitive stages. Ultrasonic testing was used to determine the damage depth, while borehole imaging was employed to reveal fracture morphology, providing complementary observations. The maximum measured fracture depth was approximately 1.9 m, which agrees well with the numerical simulations and verifies the scientific validity and reliability of the monitoring scheme.

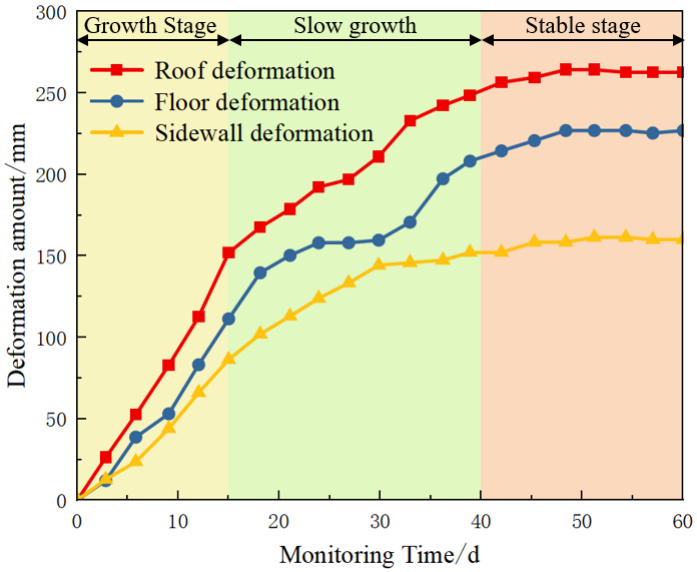

Figure 18: Deformation of the surrounding rock in the tunnel

Based on the aforementioned monitoring results, it can be concluded that when the extraction roadway is situated 17 meters below the working face floor and aligned with the working face, while being offset by 30 meters from the coal pillar, the roadway experiences minimal disturbance from mining-induced stresses. The support design for this configuration is also deemed adequate, rendering it a reasonable choice for roadway layout. The measured range of surrounding rock damage in relation to the roadway aligns well with theoretical analyses, thereby indicating that this research is both scientifically and rationally sound. This study offers theoretical support for the rational layout of extraction roadways not only in this mine but also in other mines exhibiting similar geological conditions.

6 Conclusion

(1) At the center of the working face, the vertical stress gradually approaches the original rock stress. Furthermore, as one moves away from the coal pillar on either side of the working face, the vertical stress also tends to converge towards the original rock stress. Conversely, as the distance from the floor increases, there is a general trend of decreasing vertical stress. Notably, when depth exceeds 5 meters, the rate of decrease in vertical stress becomes significantly less pronounced.

(2) The vertical stress distribution curve at various depths of the floor reveals that the stress profile in the mined-out area of the working face exhibits an "M" shape. The peak stress gradually diminishes with increasing depth below the floor, and the intensity of stress

concentration decreases as depth increases. Notably, the most significant attenuation occurs at a depth of 10 meters beneath the floor; beyond this point, the rate of attenuation declines markedly. This finding aligns with the analytical solution for the coal seam floor stress field, thereby indicating that levels greater than 10 meters below the floor represent a more appropriate selection.

(3) The maximum failure depth of the floor has been determined to be 16.51 meters. In conjunction with the vertical stress curve at various depths of the floor, it is recommended that the extraction roadway be situated at a horizontal plane 17 meters below the mined-out area. Four distinct roadway layout methods were simulated, and the results indicate that positioning the roadway 30 meters within the coal pillar produces the lowest peak in vertical stress, whereas placing it 30 meters outside of the coal pillar leads to a reduction in horizontal stress peaks.

(4) The analysis of rock mass failure characteristics across four distinct roadway positions indicates that the configuration situated 30 meters outside the coal pillar yields the smallest zone of rock mass failure. Taking into account the stress conditions of the surrounding rock, maintenance costs, and anticipated service life, it is concluded that the optimal layout for the extraction roadway should be established at a horizontal plane 17 meters below the mined-out area. This alignment should correspond with the direction of the working face and remain positioned 30 meters outside of the coal pillar.

(5) The extraction roadway at Shanxi Poly Pingshan Coal Mine is situated 17 meters below the working face floor, oriented in accordance with the direction of the working face, and offset by 30 meters from the coal pillar. Field monitoring results reveal a maximum surrounding rock failure range of 1.9 meters, which aligns with theoretical analyses. The roadway support system fulfills all necessary requirements, and no significant deformation has been observed, thereby meeting the operational demands on-site.

(6) The floor stress model, built on semi-infinite body and homogeneity assumptions, reveals an “M”-shaped distribution with only 8%–12% deviation from simulations, pinpoints a 30 m staggered coal pillar as optimal, and achieves near-perfect alignment between simulated plastic zone of 2.0 m and measured depth of 1.9 m, establishing a “theory–simulation–measurement” closed loop that delivers a robust quantitative framework for controlling deep roadway stability.

Data Availability

The datasets generated during and/or analysed during the current study are available from the corresponding author on reasonable request.

Conflicts of Interest

The authors declare no conflict of interest.

Funding Statement

This research was funded by the National Key R&D Program of China (No. 2022YFE0129100).

Author Contributions

Conceptualization, X.C. and R.M.; methodology, Y.Z.; software, Y.Z.; validation, Y.Z. and R.M.; formal analysis, Y.X.; investigation, Y.X.; resources, X.C.; data curation, X.C.; writing—original draft preparation, X.C.; writing—review and editing, R.M.; visualization, J.C.; supervision, J.L.; project administration, Y.Z.; funding acquisition, Y.Z. All authors have read and agreed to the published version of the manuscript.

References

[1] Huang Q S, Cheng J L. Research on stress distribution and failure characteristics of coal mining floor in soft-hard alternant strata [J]. Rock and Soil Mechanics, 2017, 38(S1): 36-42.

[2] Liu W T, Mu D R, Yang L, et al. Calculation method and main factor sensitivity analysis of inclined coal floor damage depth [J]. Journal of China Coal Society, 2017,42(04):849-859.

[3] Shao J, Zhang Q, Zhang W. Evolution of mining-induced water inrush disaster from a hidden fault in coal seam floor based on a coupled stress–seepage–damage model[J]. Geomechanics and Geophysics for Geo-Energy and Geo-Resources, 2024, 10(1): 1-21.

[4] Wang Y, Huang J, Wang G. Numerical analysis for mining-induced stress and plastic evolution involving influencing factors: high in situ stress, excavation rate and multilayered heterogeneity[J]. Engineering Computations, 2022, 39(8): 2928-2957.

[5] Kang H P, Gao F Q. Evolution of mining-induced stress and strata control in underground coal mines [J]. Chinese Journal of Rock Mechanics and Engineering,2024,43(01):1-40.

[6] Lu J, Jiang C, Jin Z, et al. Three-dimensional physical model experiment of mining-induced deformation and failure characteristics of roof and floor in deep underground coal seams[J]. Process Safety and Environmental Protection, 2021, 150: 400-415.

[7] Ma B W, Xie H P, Zhang X F, et al. Study on the impact failure and energy release of surrounding rock of roadway under dynamic disturbance [J]. Journal of Mining and Strata Control Engineering,2024,6(04):5-22.

[8] Wang J C, Wang Z H, Yang J, et al. Mining-induced stress rotation and its application in longwall face with large length in kilometer deep coal mine [J]. Journal of China Coal Society, 2020,45(03): 876-888.

[9] Wang H Z, Ju Y J, Qin K K, et al. A comparative study on floor failure law in deep and short-distance coal seam mining [J]. Journal of Mining & Safety Engineering,2020,37(03):553-561.

[10] Zhao C, Song W. Mechanical Models for Comparative Analysis of Failure Characteristics and Groundwater Inrush of Coal Seam Floors[J]. Applied Sciences, 2022, 12(23): 12164.

[11] Qian M G. On sustainable coalmining in China [J]. Journal of China Coal Society,2010,35(04):529-534.

[12] Zhang C, Wang J, Chang W, et al. Research on large deformation mechanism of recovery roadway under mining stress conditions[J]. Heliyon, 2024, 10(13).

[13] Zhang H L, Wang L G, Tu M, et al. Study on failure evolution laws and control technology of roadway surrounding rock under mining circumstances [J]. Journal of Mining & Safety Engineering, 2013,30(05):653-658+664.

[14] Wang L G, Han M, Wang Z S, et al. Stress distribution and damage law of mining floor [J]. Journal of Mining & Safety Engineering,2013,30(03):317-322.

[15] Luo S H, Wang T, Wu Y P, et al. Evolution characteristics of mining stress of bearing arch and interval strata in longwall mining of steeply dipping coal seam groups [J]. Journal of China Coal Society, 2023,48(02):551-562.

[16] Wang J, Ning J G, Tan Y L, et al. Deformation and failure laws of roadway surrounding rock and support optimization during shallow-buried multi-seam mining[J]. Geomatics, Natural Hazards and Risk, 2020, 11(1): 191-211.

[17] Yang S M. Numerical Simulation Study on Reasonable Horizon of Floor Drainage Roadway in Yian Mine [J]. Safety in Coal Mines, 2015, 46(06): 164-166.

[18] Zhao C, Cheng Z H, Kong D Z, et al. Study on Stress Distribution of Floor and Gas Drainage

Technology in Downward Mining of Close Distance Coal Seam Group [J]. Coal Engineering, 2019, 51(07): 109-113.

[19] Tang Z, Ai D C, Peng B, et al. Optimum Analysis of Floor Gas Extraction Roadway Location in Gassy Mine Based on FLAC3D [J]. Mining Safety & Environmental Protection, 2015, 42(02): 88-91.

[20] Liu Z W, Zhang S. Study on rational layout of floor gas drainage gateway in high gassy—outburst seam [J]. Coal Science and Technology, 2018, 46(10): 155-160.

[21] Li Y E, Ma N J, Ma J, et al. Surrounding rock's failure characteristic and rational location of floor gas drainage roadway above deep confined water [J]. Journal of China Coal Society, 2018, 43(09): 2491-2500.

[22] Zhang H L, Wang L G. Computation of Mining Induced Floor Additional Stress and Its Application [J]. Journal of Mining & Safety Engineering, 2011, 28(02): 288-292+297.

[23] Liu W T, Mu D R, Yang L, et al. Calculation method and main factor sensitivity analysis of inclined coal floor damage depth [J]. Journal of China Coal Society, 2017, 42(04): 849-859.

[24] Fan, Z.; Song, X.; Wang, D.; Ayasrah, M.; Li, S. Poroelastic Solutions of a Semi-Permeable Bore-hole Under Non-Hydrostatic In Situ Stresses Within Transversely Isotropic Media[J]. Int. J. Geomech. 2025, 25, 04024342.

[25] Gao, R.; Kuang, T.; Meng, X.; Huo, B. Effects of ground fracturing with horizontal fracture plane on rock breakage characteristics and mine pressure control[J]. Rock Mech. Rock Eng. 2021, 54, 3229–3243.

[26] Gao, R.; Dou, B.; Yu, B.; Yang, T.; Meng, X.; Zhang, W. Ground fracturing of multi-strata for strong ground pressure control in extra-thick coal seams with hard roofs: Numerical simulation and case study[J]. Eng. Fract. Mech. 2024, 303, 110129.

[27] Zhang, X., Li, J.. Advancements and challenges of high-speed active flow control: Plasma actuators[J]. International Journal of Heat and Mass Transfer, 252, 127481.

[28] Li, J., Zhang, X. Active flow control for supersonic aircraft: A novel hybrid synthetic jet actuator[J]. Sensors and Actuators A: Physical, 302, 111770.

[29] Shaoyi Jiang, Jiahui Zhang, Kailin Diao, Xiaomin Liu, Zhezheng Ding. Research Advances in Solvent Extraction of Lithium: The Potential of Ionic Liquids[J]. Advanced Functional Materials, 2025, 35(29), 2423566.